Check for updates

Methylxanthines for halogen bonded cocrystals with 1,4-diiodotetrafluorobenzene: green synthesis, structure, photophysics and DFT studies†

Mónica Benito, [iD] *[a] Rosario Núñez, [iD] *[a] Sohini Sinha, [iD] ‡[a] Claudio Roscini, [iD] [b] Yoan Hidalgo-Rosa,[c] Eduardo Schott,[d] Ximena Zarate*[e] and Elies Molins [iD] [a]

Four new halogen-bonded cocrystals of biological methylxanthines, named caffeine, theophylline and theobromine, have been prepared with 1,4-diiodotetrafluorobenzene as a halogen bond donor by mechanochemical and solution processes. For theophylline, N⋯I and N⋯O interactions were observed, while for caffeine and theobromine, only N⋯I was detected. The solids were characterized by PXRD, SC-XRD, FTIR and thermal methods (TGA-DSC analyses). In addition, the solid-state photoluminescence properties of the methylxanthines and their respective cocrystals have been studied and quantum chemistry calculations have been performed to rationalise and understand the electronic and optical properties of all compounds. This work provides a triad of natural methylxanthines capable of forming halogen-bonded multicomponent systems that can give rise to a cocrystal-to-crystal transformation with off–on luminescence activation.

Introduction

Mechanochemistry, and by extension reactive extrusion, has been identified by IUPAC among the ten top emerging technologies that will change the world to make it more sustainable.[1] Some of the advantages of the mechanochemical

[a] *Institut de Ciència de Materials de Barcelona (ICMAB-CSIC), Campus UAB, 08193 Bellaterra, Barcelona, Spain. E-mail: mbenito@icmab.es, rosario@icmab.es*

[b] *Catalan Institute of Nanoscience and Nanotechnology (ICN2), CSIC and The Barcelona Institute of Science and Technology (BIST), Campus UAB, Bellaterra, Barcelona 08193, Spain*

[c] *Centro de Nanotecnología Aplicada, Facultad de Ciencias, Ingeniería y Tecnología, Universidad Mayor, Camino La Pirámide 5750, Huechuraba, Santiago, 8580745, Chile*

[d] *Departamento de Química Inorgánica, Facultad de Química y Farmacia, Centro de Energía UC, Centro de Investigación en Nanotecnología y Materiales Avanzados CIEN-UC, Pontificia Universidad Católica de Chile, Avenida Vicuña Mackenna, 4860 Santiago, Chile*

[e] *Instituto de Ciencias Aplicadas, Facultad de Ingeniería, Universidad Autónoma de Chile, Av. Pedro de Valdivia 425, Santiago, Chile. E-mail: ximena.zarate@uautonoma.cl*

† Electronic supplementary information (ESI) available: Additional information concerning hydrogen-bond interactions of the new compounds, FT-IR spectra, TGA-DSC thermograms, a structural model used in the calculations, computed values of selected bond lengths (Å) for cocrystals, frontier molecular orbitals of methylxanthines (caffeine, theophylline and theobromine) and their cocrystals, molecular orbitals located on the analyte that is involved in the electronic transitions of caffeine, theobromine and theophylline-DITFB cocrystals are included. CCDC numbers 2304676–2304678. For ESI and crystallographic data in CIF or other electronic format see DOI: https://doi.org/10.1039/d4ce00138a

‡ Present address: Catalan Institute of Nanoscience and Nanotechnology (ICN2), CSIC and her email: sohini.sinha@icn2.cat

process include the avoidance of large amounts of solvent, quantitative reactions, reduction of waste products, generally shorter time-scale compared to other solvent-based approaches, and mild temperatures. All these benefits have allowed the use of grinding processes in many different areas of application that range from metallurgic to organic synthesis, catalysis or crystal engineering.[2–5]

Crystal engineering has been a considerable tool for tuning the physical properties of compounds. Among supramolecular materials, cocrystals are defined as a class of multicomponent solids wherein neutral components bonded by non-covalent interactions, including hydrogen and halogen bonds, among others, are present within a crystalline compound in a stoichiometric ratio. The halogen bond has been defined as "a neat attractive interaction between an electrophilic region (σ-hole) associated with a halogen atom in a molecular entity and a nucleophilic region in another, or the same, molecular entity".[6] The halogen bond is also present in biological systems such as protein–ligand systems used in drug delivery. A few iodinated thyroid hormones (thyroxines T4 and T3) are known to behave as halogen-bond donors. Many active pharmaceutical ingredients (APIs) have been designed to contain halogenated atoms in their backbone, not only to provide steric hindrance but also to improve their lipophilicity, which helps to penetrate the cellular membranes and tissues.[7,8]

In the last few years, some of us have studied the propensity of different modified nucleobases for the preparation of

multicomponent solids (salts and cocrystals) containing both hydrogen and halogen bonds.[9–12] Now we study xanthines, which are indeed purine-based nitrogen compounds with a structure similar to that of DNA bases adenine and guanine and their related nucleotides. This even makes them important scaffolds for the exploration of new potential drugs.[13] Moreover, some natural methylxanthines, such as caffeine (**CAF**), theophylline (**TPH**), and theobromine (**TBR**), are compounds extracted from medicinal plants. While caffeine (1,3,7-trimethylxanthine) is a trimethylated derivate, theophylline (1,3-dimethylxanthine) and theobromine (3,7-dimethylxanthine) are dimethylated and structural isomers, the main difference being the second methyl group at the C1 or C7 position, respectively (see Chart 1). All of them are recognized for their pharmaceutical applications and biological effects.[14,15]

The crystal engineering of these methylxanthines based on hydrogen-bond interactions is a thoroughly explored area. However, to the best of our knowledge, the preparation and structural study of new crystalline solid forms from them, through halogen bonding interactions, has not been reported yet. Therefore, it remains unexplored how the halogen bond interactions between the methylxanthine and a coformer can influence the crystal structure and their physico-chemical properties. In this study, the well-known halogen-bond donor and ditopic 1,4-diiodotetrafluorobenzene (**DITFB**, see Chart 1) has been chosen as a coformer for cocrystal screening.

In the last decades, the development of new materials has opened up exciting opportunities for modulating and enhancing photoluminescence (PL) properties for various applications. Although traditionally PL has been mainly studied in molecular systems that contain both electron-donor and electron-acceptor moieties,[16] more recently, the interest has focused on the modulation of luminescence in the solid state by self-assembly through molecular interactions.[17] In the particular case of cocrystals, progressive advances have been reported following the preparation of halogen bonded cocrystals.[18–26] Concerning the PL properties of methylxanthines, little information has been found in the literature; while some references to phosphorescence in solution have been reported in the past,[27–34] solid state studies are very scarce[34] and specific for caffeine or theobromine derivatives.[35,36] On the other hand, the use of **DITFB** as a coformer in combination with fluorescent organic compounds or aromatic model systems has afforded new cocrystals with luminescence features (fluorescence and phosphorescence) in the solid state.[18,19,21,23–26] However, it is desirable to extend these studies to understand the fundamental mechanisms of the luminescence process and find suitable, cheap and really accessible molecules for solid-state fluorescent materials, as well as new applications.

With this idea in mind, in the present work, new cocrystals from these natural methylxanthines and **DITFB** have been prepared by liquid-assisted grinding (LAG). Crystal structure analysis indicates that these precursors can form 1:1, 2:1 or even 4:1 molar ratio cocrystals through halogen bonds. Herein, their physical characterization by thermal analysis and spectroscopic techniques including FTIR, UV-vis and solid-state emission spectroscopy has been described. Time-dependent density functional theory (TD-DFT) studies were used to understand the change in the luminescence properties of the cocrystals with respect to the parent compounds.

Experimental section

All reagents were from commercial sources and used without further purification. Analytical grade solvents were used for the crystallization experiments.

Liquid-assisted grinding

Mechanochemical synthesis of cocrystals were performed using a Retsch mixer mill MM400 in 10 mL agate grinding jars with two 5 mm agate balls. Variable amounts (stoichiometric ratios 1:1, 2:1 or 4:1) of the selected methylxanthine and the coformer **DITFB** were ground for 30 min at 30 Hz upon addition of two drops of the chosen solvent. To avoid any confusion it should be pointed out that only the methylxanthine:DITFB molar ratio, when two cocrystals have been obtained, is included in the naming of the new cocrystals.

Details for each multicomponent system are described below.

CAF-DITFB. A mixture of caffeine (form β, refcode: NIWFEE03[37]) (100.01 mg, 0.52 mmol) and **DITFB** (51.78 mg, 0.13 mmol) was placed in the grinding jar with two drops of methanol. The mixture was milled for 30 min at 30 Hz. Needle-shaped single crystals were obtained by slow evaporation of a methanol solution of the ground solid at room temperature.

TPH-DITFB. A mixture of theophylline (form II, refcode BAPLOT01[38]) (75.08 mg, 0.416 mmol) and **DITFB** (167.27 mg, 0.416 mmol) was placed in the grinding jar with two drops of
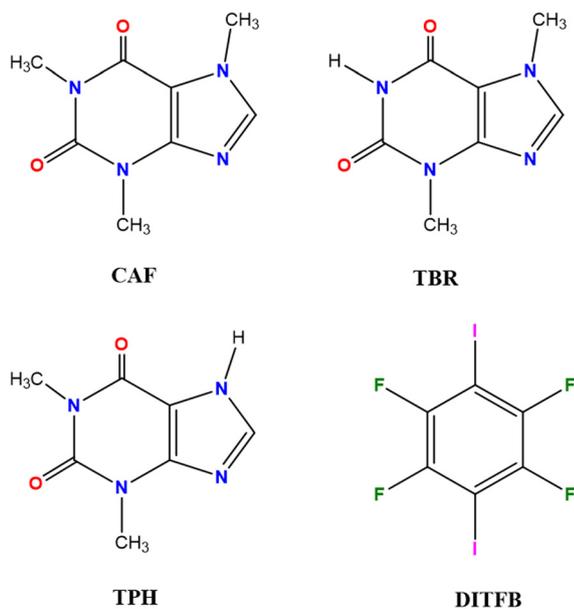
Chart 1 Chemical structures of natural methylxanthines and DITFB used in this work.

methanol. The mixture was milled for 30 min at 30 Hz. This solid was used for growing good quality crystals in methanol by slow evaporation at room temperature.

TBR-DITFB (1 : 1). A mixture of theobromine (refcode: SEDNAQ[39]) (75.01 mg, 0.416 mmol) and **DITFB** (167.24 mg, 0.416 mmol) was placed in the grinding jar with two drops of methanol. The mixture was milled for 30 min at 30 Hz yielding a crystalline solid.

TBR-DITFB (2 : 1). A mixture of **TBR** (100.11 mg, 0.555 mmol) and **DITFB** (111.72 mg, 0.278 mmol) was placed in the grinding jar with two drops of nitromethane. The mixture was milled for 30 min at 30 Hz and yielded a crystalline solid. The solid obtained using the same amounts of **TBR** and **DITFB** in methanol and the same conditions was used for growing single crystals by heating in a mixture of methanol–dimethylsulfoxide (DMSO) and ethanol (1 : 1 : 10). The solution was filtered using a syringe filter (nylon, 0.2 μm) and allowed to evaporate slowly at rt. Needle-type crystals were obtained after 4 weeks.

Powder X-ray diffraction (PXRD)

PXRD data were collected using a Siemens D5000 powder X-ray diffractometer with Cu-Kα radiation (λ = 1.5418 Å), with

40 kV and 39 mA voltage and current applied. An amount of powder was gently pressed on a glass slide to afford a flat surface and then analyzed. The samples were scanned in the 2θ range of 2–50° using a step size of 0.02° and a scan rate of 1 s per step.

Single crystal X-ray diffraction (SC-XRD)

Single crystals of compounds **CAF-DITFB**, **TPH-DITFB** and **TBR-DITFB** (2 : 1) were selected and mounted for X-ray single crystal diffraction experiments. Crystallographic data were collected on a Bruker APEX-II CCD diffractometer using graphite monochromated Mo Kα radiation (λ = 0.71073 Å). Crystallographic data were collected at 294(2) K. Data reduction was performed using SAINT V6.45A, SORTAV,[40] and SADABS[41] in the diffractometer package. The structural resolution procedure was made using SHELXT[42] and the refinement by least squares on F^2 was performed using SHELXL2014/7 inside the WinGX program environment.[43,44] For **CAF-DITFB**, although several crystallizations were performed and after checking different crystals, the best dataset for **CAF-DITFB** was selected for the X-ray study. A major component was integrated, although other minor components were observed in the frame images. The full set

Table 1 Crystallographic data and structural refinement parameters for compounds **CAF-DITFB**, **TPH-DITFB** and **TBR-DITFB** (2 : 1)

Compound	CAF-DITFB	TPH-DITFB	TBR-DITFB (2 : 1)
Empirical formula	C19 H20 F2 I N8 O4	C13 H8 F4 I2 N4 O2	C20 H16 F4 I2 N8 O4
Formula weight	589.33	582.03	762.21
Temperature (K)	294(2)	294(2)	294(2)
Crystal system	Monoclinic	Monoclinic	Triclinic
Space group	$P2_1/c$	$P2_1/n$	$P\bar{1}$
Unit cell dimensions	a = 21.904(18) Å	a = 19.924(8) Å	a = 4.0269(18) Å
	b = 4.044 (4) Å	b = 4.4267(18) Å	b = 7.451(3) Å
	c = 25.87(2) Å	c = 20.419(8) Å	c = 20.660(9) Å
	α = 90°	α = 90°	α = 82.022(8)°
	β = 110.90(2)°	β = 113.293(9)°	β = 88.669(8)°
	γ = 90°	γ = 90°	γ = 80.671(9)°
Volume (Å³)	2140(3)	1654.1(11)	605.8(5)
Z	4	4	1
Density calc. (mg m⁻³)	1.829	2.337	2.089
Absorption coefficient (mm⁻¹)	1.561	3.860	2.673
F(000)	1172	1088	366
Crystal size (mm³)	0.32 × 0.07 × 0.06	0.28 × 0.05 × 0.02	0.12 × 0.08 × 0.07
Theta range for data collection (°)	1.623 to 28.944	1.837 to 28.019	1.991 to 28.506°
Index ranges	−29 <= h < 29,	−26 <= h <= 26,	−5 <= h <= 5,
	−5 <= k <= 5,	−5 <= k <= 5,	−9 <= k <= 9,
	−34 <= l <= 35	−26 <= l <= 26	−27 <= l <= 27
Reflections collected	58 277	32 965	12 902
Independent reflections	5576 [R(int) = 0.3691]	3979 [R(int) = 0.0509]	3074 [R(int) = 0.0698]
Completeness to θ max (%)	100.0%	100.0%	100%
Max. and min. transmission	1 and 0.54	1 and 0.695	1 and 0.618
Refinement method	Full-matrix least-squares on F^2		
Data/restraints/parameters	5576/0/313	3979/0/228	3074/0/174
Goodness-of-fit on F^2	0.970	1.021	1.008
Final R indices [$I > 2\sigma(I)$]	R_1 = 0.0715,	R_1 = 0.0306,	R_1 = 0.0529,
	wR_2 = 0.1398	wR_2 = 0.0676	wR_2 = 0.1238
R indices (all data)	R_1 = 0.1566,	R_1 = 0.0453,	R_1 = 0.0850,
	wR_2 = 0.1686	wR_2 = 0.0748	wR_2 = 0.1410
Largest diff. peak and hole (e Å⁻³)	1.095 and −0.936	0.568 and −0.798	1.199 and −1.623
CCDC no.	2304678	2304676	2304677

of data was used in the refinement (even the high R_{int} value), which afforded the best results with a reasonable quality of the final crystal structure. Non-hydrogen atoms were refined with anisotropic atomic displacement parameters. Hydrogen atoms were introduced in calculated positions and refined riding on their parent atoms. Selected crystal and data collection parameters are reported in the corresponding Table 1.

Mercury 2021.1.0 software was also used to calculate the PXRD powder patterns of the new cocrystals based on the single-crystal X-ray structures and to predict the Bravais, Friedel, Donnay and Harker (BFDH) morphology using the CSD Materials module.[45]

Complete crystallographic data for the structural analysis have been deposited to the Cambridge Crystallographic Data Centre, CCDC no. 2304676–2304678.

Thermogravimetric analysis – differential scanning calorimetry (TGA-DSC)

A simultaneous thermogravimetric analysis (TGA)-differential scanning calorimetry/differential thermal analysis (heat flow DSC/DTA) system NETZSCH-STA 449 F1 Jupiter was used to study the thermal properties of the solids. Samples (3–8 mg) were placed in an open alumina pan and measured at a scan speed of 10 °C min^{-1} from ambient temperature to 300 °C under a N_2 atmosphere as protective and purge gas (their respective flow velocities were 20 and 40 mL min^{-1}).

Spectroscopic measurements

A Jasco 4700LE spectrophotometer with an attenuated total reflectance accessory was used to record the FT-IR spectra of the starting products and the new cocrystals in the range from 4000 to 400 cm^{-1} and at a resolution of 4.0 cm^{-1} and 32 scans. Fluorescence images were taken using an Olympus BX51 microscope with a DP20 camera and a mercury lamp U-RFL-T accessory for the sample excitation in the UV-visible region. Diffuse reflectance analyses were performed using a Jasco UV-vis-NIR V-780 spectrophotometer with a diffuse reflectance sphere accessory in the scan range of 200–800 nm. The diffusion reflectance was converted in the $F(R)$ function through the Kubelka–Munk law. Steady-state luminescence spectra and fluorescence quantum yields for all the compounds in the solid state were measured on a Hamamatsu absolute PL quantum yield spectrometer C9920-02G.

Theoretical calculations

Periodic models of cocrystals. To simulate the extended structures of the cocrystals, periodic density functional theory (periodic-DFT) calculations were performed. All periodic calculations were carried out using the Perdew–Burke–Ernzerhof (PBE)[46] functional and projected augmented wave (PAW) PSlibrary v1.1.0 pseudopotentials,[47] considering 60 Ryd as the energy-cutoff and 400 Ryd as the density cutoff. The cell optimization process is considered as free lattice

vectors and coordinate optimization. An empirical dispersion correction was also applied to all calculations under the Grimme-D3 (DFT-D3) scheme.[48,49] Particularly, a $2 \times 2 \times 3$ k-point scheme was employed to optimize the crystal experimental model. All calculations were performed using the Quantum Espresso 7.0 package.[50] In the second stage, the simulation was carried out by extracting a fraction of the crystal (finite fragment) and treating it with more robust methodologies, as implemented in molecular modeling software. The purpose of this procedure was to obtain the electronic configuration of the system in both the ground state (S_0) and the excited states (S_1 and T_1). This procedure allowed the simulation of the electronic and optical properties therefore using levels of theory that are not currently available for the periodic calculations.

Molecular model (finite fragments) of cocrystals. All calculations were performed with the ORCA 5.0.3 code.[51] The molecular models for the simulation of cocrystals were designed based on the crystal optimized *via* periodic-DFT. With respect to methylxanthine and the coformer **DITFB**, the stoichiometry for these molecular models was $1:1$, $2:1$, or $4:1$ for **TPH-DITFB**, **TBR-DITFB** ($2:1$), and **CAF-DITFB**, respectively. The initial configuration was derived from the optimized crystal structure of each of these cocrystals. (see Fig. S1a†). In the case of free methylxanthine, the structural model for the simulations was created using the available crystallographic data for caffeine, theophylline, and theobromine (see Fig. S1b†).

The electronic structure for all the electronic states (S_0, S_1 and T_1) were computed using the Perdew–Burke–Ernzerhof (PBE) function[52] and the basis set def2-TZVPP.[53,54] The ma-def2-SVP basis set with the Def2-ECP pseudopotentials was used to treat iodine atoms. The RIJ approach for the Coulomb term with the "chain of spheres" COSX approximation and their related auxiliary basis sets were used to speed up the SCF computation.[55,56] A time-dependent DFT (TD-DFT) method[51] was used to simulate the optical properties (absorption) of all compounds. The PBE0[57] hybrid exchange correlation and the def2-TZVPP[53] basis set were used to compute the absorption spectra for all systems.

Results and discussion

Synthesis of cocrystals and powder X-ray diffraction

Liquid-assisted grinding was used as a fast and reliable method for solid phase screening. To confirm the phase purity of the bulk solid obtained by LAG, powder X-ray diffraction analysis was performed for all the samples. The results are shown in Fig. 1 and 2. New phases were obtained for **CAF** or **TPH** when co-crystallized with the donor coformer in the presence of methanol, in $4:1$ (**CAF-DITFB**) and $1:1$ (**TPH-DITFB**) molar ratios, respectively. Further, the peak positions were correlated with the corresponding simulated powder patterns from the crystal structures for these two compounds confirming the great agreement for all of them (Fig. 1a and b, respectively).
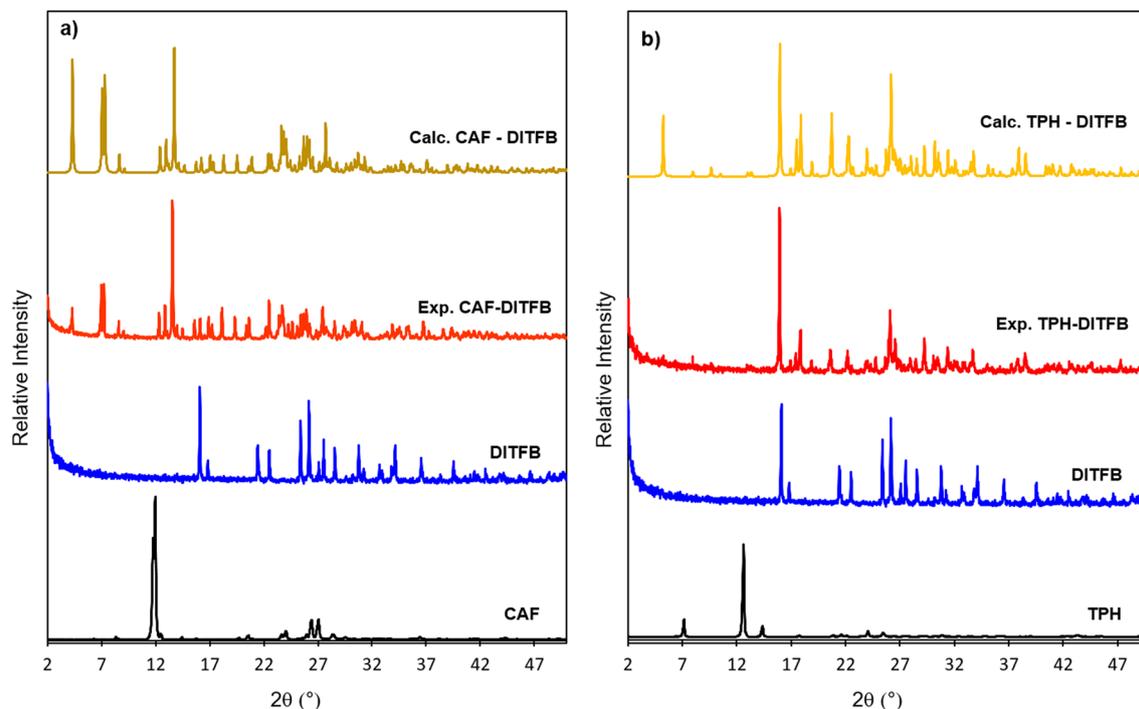
Fig. 1 PXRD patterns of former compounds and the new cocrystals (experimental and calculated from crystal structures) for a) **CAF–DITFB** and b) **TPH–DITFB** systems.
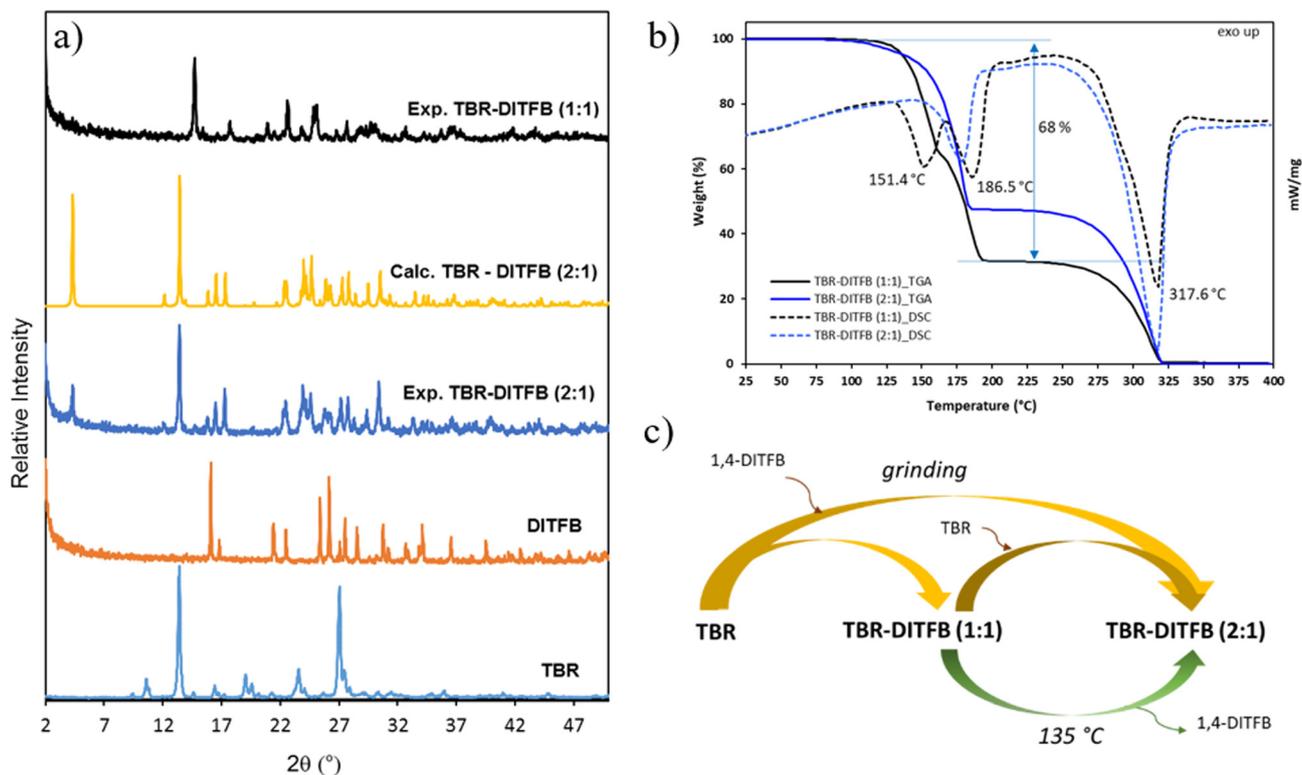

Fig. 2 a) PXRD patterns of starting materials (**TBR** and **DITFB**) and the new cocrystals (experimental and calculated from crystal structures); b) TGA (solid lines)–DSC (dashed lines) traces of cocrystals **TBR-DITFB** (1:1) and **TBR-DITFB** (2:1) and c) phase transformations among **TBR** and its cocrystals.

In the case of the **TBR-DITFB** system, the grinding process at a 1:1 ratio, with a few drops of methanol, afforded the cocrystal **TBR-DITFB** (1:1), as suggested by a powder pattern, which was different from the pristine compounds. On the other hand, grinding **TBR-DITFB** at a 2:1 ratio, the process did not proceed effectively as the powder pattern of the bulk solid contained a mixture of the same phase observed previously for the **TBR-DITFB** (1:1) system, along with the phase corresponding to the starting **TBR**.

Surprisingly, when the process was carried out in nitromethane, chloroform, or dichloromethane as catalytic solvents, the process was quantitative and a new phase, corresponding to the cocrystal **TBR-DITFB** (2:1), was yielded, as shown in Fig. 2a.

Finally, from a mixture of methanol, EtOH and DMSO, it was possible to isolate single crystals of the corresponding new **TBR-DITFB** (2:1) cocrystal.

Unfortunately, despite the efforts performed to isolate single crystals of the **TBR-DITFB** (1:1) cocrystal, they could not be obtained. **TBR** showed very low solubility in many common solvents and in all cocrystal syntheses a residual part of non-cocrystallized **TBR** was always found even when working in an excess of **DITFB**. This was ascribed to the different solubility between **TBR** and **DITFB** and the thermal stability of the cocrystals, as it will be commented later in the thermal analysis section.

Structural description of single crystals

Cocrystal **CAF-DITFB** crystallizes in the monoclinic space group $P2_1/c$ with two different molecules of caffeine and half a molecule of **DITFB** in the asymmetric unit (Fig. 3a). At first sight, self-assembled caffeine molecules are linked through hydrogen bonds established between the carbonyl groups and C–H groups as no N–H moieties are available in this trimethylated xanthine. This yields zigzag chains, which are also bridged by halogen bonds with the coformer through N···I interactions (Fig. 3c). Additionally, zig-zag chains of
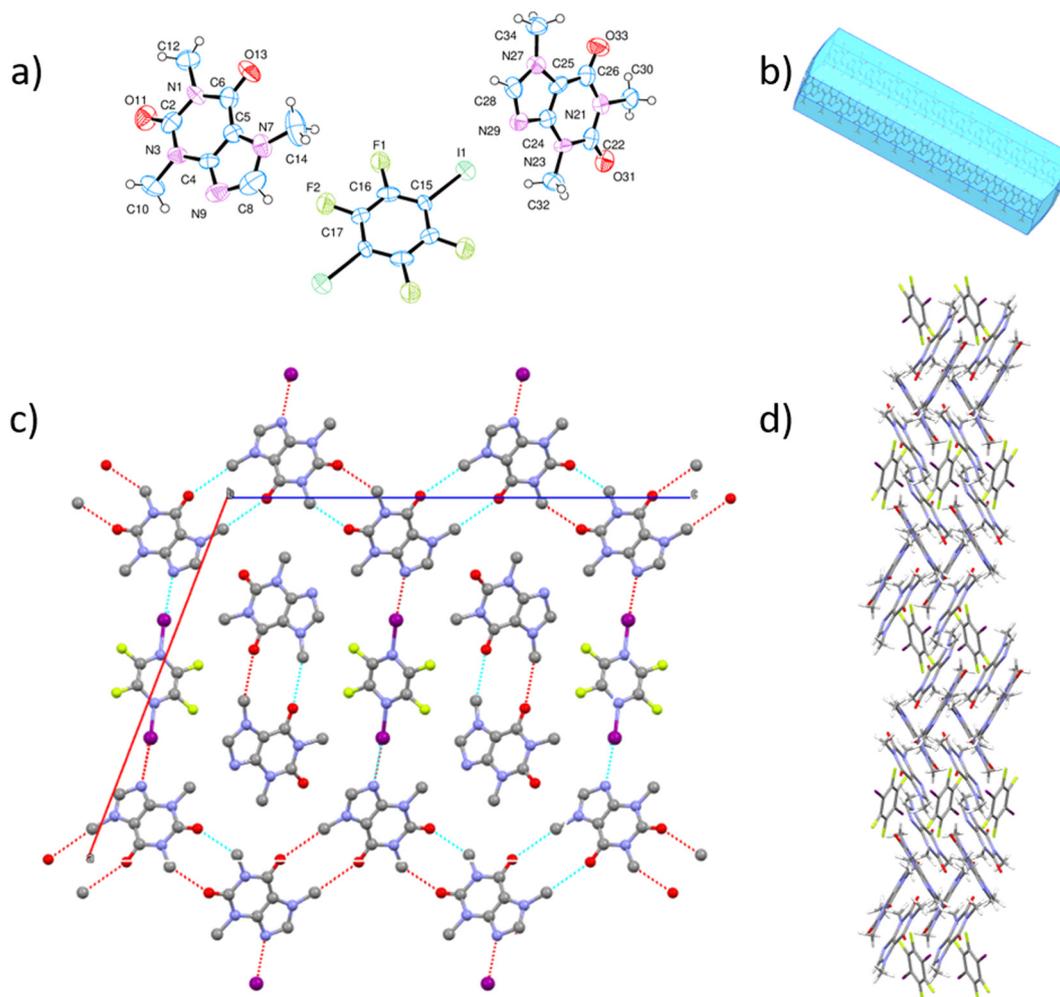
Fig. 3 a) ORTEP with atom numbering. Note only half of the **DITFB** molecule contains atom labelling, indicating the equivalence of the other half, and thus, giving a 4:1 molar ratio, b) BFDH predicted morphology, c) hydrogen and halogen bonding interactions in the packing (view along the *b* axis). Additionally, self-assembly of other caffeine molecules giving a zigzag chain, and d) perspective view along the *a* axis of cocrystal **CAF-DITFB**.
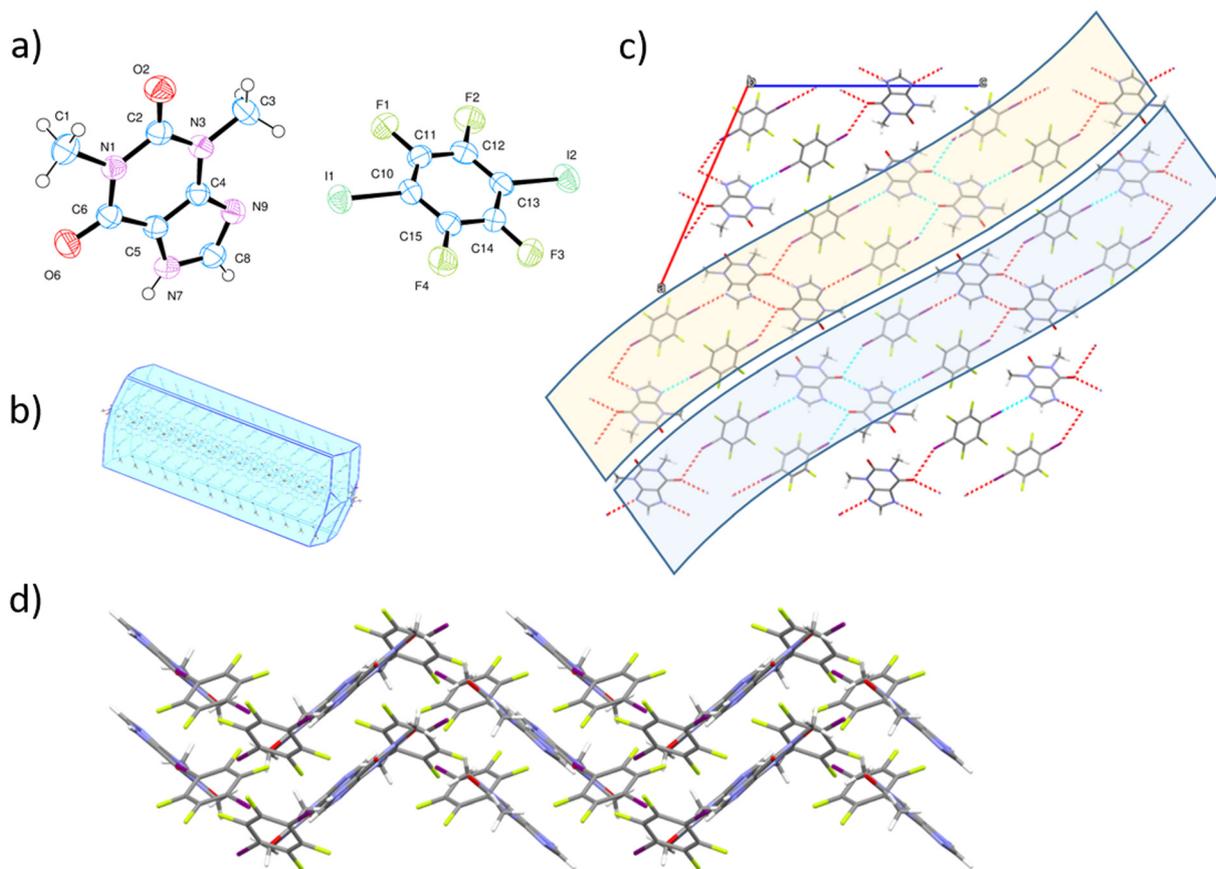
Fig. 4 a) ORTEP with atom numbering, b) BFDH predicted morphology, c) hydrogen and halogen bonds in tapes along the *b* axis and d) tapes (perspective view along the *c* axis) of cocrystal **TPH-DITFB**.

caffeine molecules are also assembled like in DNA. All these interactions are the responsible for the final 4:1 molar ratio observed in the **CAF-DITFB** cocrystal, showing a needle habit in agreement with the BFDH predicted morphology (Fig. 3b and d). Although not very common, recently we reported another cocrystal containing the same molar ratio with 5-fluorouracil and **DITFB**.[12]

Compound **TPH-DITFB** crystallizes from a methanol solution as needles, in agreement with the BFDH predicted morphology (Fig. 4b), in the monoclinic space group $P2_1/n$, with one molecule of **TPH** and one molecule of the ditopic coformer (Fig. 4a). **TPH** molecules are self-assembled by hydrogen bonds between C=O(6)···H(7)–N(7) atoms. Each **TPH** molecule in the dimer is bridged to two molecules of **DITFB** through halogen bonds by the same carbonyl group (C=O(6)···I(2)) as well as by N(9)···I(1) interactions, leading to twisted tapes (Fig. 4c). These tapes are interconnected through the C(1)–H(1A)···O(2) and C(1)–H(1B)···O(2) hydrogen bonds and C(3)–H(3A)···I(1) and C(3)–H(3B)···I(2) halogen bond interactions which afford the final tridimensional packing. Distances and angles for the halogen bond interactions observed for these two cocrystals, **CAF-DITFB** and **TPH-DITFB**, are shown in Table 2, while H-bond interactions are summarized in Table S1 in the ESI.†

Cocrystal **TBR-DITFB** (2:1) also crystallized as needles from a methanol solution in agreement with the BFDH predicted morphology (see Fig. 5a). It belongs to the triclinic space group $P\bar{1}$, with one molecule of **TBR** and half a molecule of the halogen bond donor coformer in the asymmetric unit, Fig. 5b. In this case, self-assembly between two **TBR** molecules is also observed through the hydrogen bond interactions N(1)–H(1)···O(6), C(7)–H(7A)···O(2) and C(7)–H(7C)···O(6), which yielded zigzag tapes of **TBR** molecules. These are bridged by only one type of halogen bond between N(9) and I(1) atoms through the N(9)···I(1) interaction (see Table 2 for distances and angles), forming first a folded structure which resembles a ladder where the **TBR** molecules represent its steps (see Fig. 5c). Finally, the

Table 2 Halogen bond interaction with distances and angles for the new cocrystals

Cocrystal	I···A^a	d(I···A) (Å)	(C–I···A) (°)
CAF-DITFB	I(1)···N(29)	2.859(8)	175.0(2)
TPH-DITFB	I(1)···N(9)	2.979(4)	177.23(11)
	I(2)···O(6)^i	3.392(3)	152.36(12)
TBR-DITFB (2:1)	I(1)···N(9)	3.032(5)	176.1(2)

^{a} A: Halogen bond acceptor. ^{i}1/2 + x, 1/2 − y, −1/2 + z.
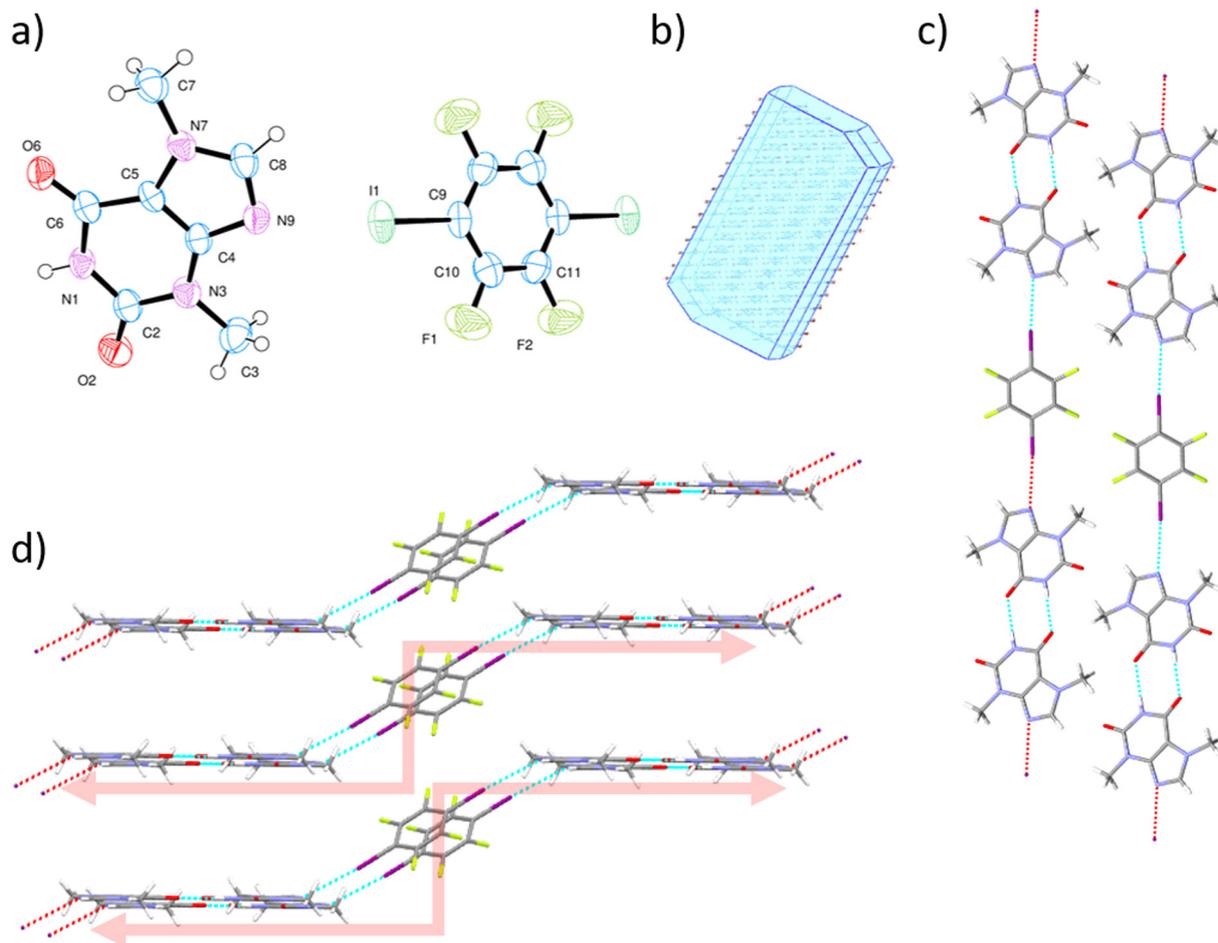
Fig. 5 a) ORTEP with numbering. Note only half of the **DITFB** molecule contains atom labelling, indicating the equivalence of the other half, and thus, giving a 2 : 1 molar ratio, b) BFDH predicted morphology, c) hydrogen and halogen bonds in tapes and d) perspective view of the ladders of cocrystal **TBR-DITFB** (2 : 1).

tridimensional packing is promoted by additional F⋯F interactions between **DITFB** molecules from different chains, F⋯H–C interactions with the methyl groups of **TBR**, and π–π stacking between coformer rings or xanthine molecules (Fig. 5d).

Thermal analysis

The thermal behavior of the new cocrystals and the starting materials was studied by simultaneous TGA-DSC. No mass loss was observed before melting, confirming that the four cocrystals are unsolvated and with the component ratio confirmed by SC-XRD. In Table 3 the melting points (Mp) of precursors and cocrystals are collected. The DSC trace for cocrystal **CAF-DITFB** shows two endothermic peaks at T_{peak} = 165.9 and 236.6 °C. The loss weight of 31% observed up to approximately 170 °C was associated with the removal of the donor coformer (theoretical amount of weight 34.1%) of the 4 : 1 **CAF-DITFB** cocrystal. A second step of 67% weight loss, corresponding to the endo peak of the DSC trace at 236 °C, was ascribed to the melting-decomposition of caffeine (Mp = 236 °C, from the literature) (Fig. S2†).[58]

For cocrystal **TPH-DITFB**, in the DSC, two sharp endothermic peaks were observed, at a T_{peak} of 148.0 °C, with a wide shoulder at 164.8 °C, and 271.5 °C (Fig. S3†). The weight loss measured (68.9%) in the TGA analysis in agreement with the first event at 148.0 °C, matches well with the removal of a molecule of **DITFB** (theoretical weight amount of 69%). The latter endothermic peak corresponds to the melting decomposition of TPH (Mp = 273 °C).[54]

In the DSC of the compound **TBR-DITFB** (1 : 1), two endothermic peaks at around 151.4 and 186.5 °C were observed and the TGA trace suggests a two-step weight loss (68% in total) ascribed to the removal of the halogenated

Table 3 Summary of melting points (Mp) of natural methylxanthines, coformer and the synthesized cocrystals

Compound	Mp (°C)	Cocrystal	T_{peak} (°C)
DITFB	108–110		
CAF	236	**CAF-DITFB**	165.9 and 236.6
TPH	273	**TPH-DITFB**	148.0, 164.8 and 271.5
TBR	357	**TBR-DITFB** (1 : 1)	151.4, 186.5 and 317.6
		TBR-DITFB (2 : 1)	178.1 and 317.5

coformer (Fig. 2b). The last endothermic signal (at 317.6 °C) was attributed to the decomposition of **TBR**.[59]

Finally, the TGA-DSC for compound **TBR-DITFB** (2:1) showed a single endothermic peak at 178.1 °C with the expected weight loss of 52.4%, corresponding to the weight of the **DITFB** coformer.

Phase transformations

Phase transformation between cocrystals with different stoichiometric ratios are scarcely studied although a few examples have been described in the literature.[60–62] Interestingly, these multicomponent solids are expected to show different physical properties depending on the phase, which extends the plethora of the properties of the solid forms available.

In view of our results, we aimed to study the relationship between **TBR** and its cocrystals (**TBR-DITFB** (1:1) and (2:1)) and their interconversion through grinding or sublimation, as shown in Fig. 2c. When the two precursors (**TBR** and **DITFB**) were ground together using the appropriate molar ratio (1:1 or 2:1) and solvent (methanol or chloroform, respectively), two different cocrystals were obtained. Also, solid phase transformation from the cocrystal **TBR-DITFB** (1:1) to the cocrystal **TBR-DITFB** (2:1) was possible upon the extra addition of **TBR** while grinding in chloroform. In methanol, a mixture of both cocrystals resulted from the extra addition of **TBR**. On the other hand, by heating the **TBR-DITFB** (1:1) cocrystal at 135 °C, the formation of long needles at the top of the vial was observed, which through single-crystal X-ray diffraction were assigned to the halogenated coformer **DITFB**.

In a similar way, by heating compounds **CAF-DITFB** and **TPH-DITFB** at 165 °C and 130 °C, respectively, long needles were noticed at the top of the vial, which were ascribed to the **DITFB** compound (Fig. S4†). The residual solid was further analyzed by PXRD and the observed phases confirmed the presence of the precursors **β-CAF** along with some remaining cocrystal or **TPH** form II. This result confirmed that for **TPH** the **TPH-DITFB** (2:1) cocrystal could not be obtained (Fig. S3b†).

FT-IR spectroscopic analysis of cocrystals

FT-IR was performed to i) corroborate the presence of both components, *i.e.* methylxanthines and **DIFTB** and to ii) ensure the presence of hydrogen and halogen bonds in the cocrystals, taking advantage of the variation of their more characteristic vibrational modes. The vibrational modes for the free coformer **DIFTB** appeared at 1456 (vC–C stretching aromatic ring), 937 (vC–F stretching) and 755 (vC–I asymmetric stretching) cm^{-1}. Some of these stretching modes appeared slightly shifted in the FT-IR spectra of the new cocrystals (see Fig. S5 and Table S2†) suggesting the existence of N⋯I and O⋯I interactions already observed by SC-XRD.

For the methylxanthines, the changes of C=O, C=N and N–H modes were examined.

By careful analysis of the single-crystal structure of the starting **β-CAF**, no H-bonds could be detected, while π–π stacking and other short interactions were present. In the cocrystal **CAF-DITFB**, higher wavenumbers for the C=O and C=N modes were recorded, suggesting that some kind of new interaction for these functional groups has taken place. SC-XRD showed that self-assembly occurred through the carbonyl and C–H groups. The halogen bonds between the only available nitrogen, N(27), and the ditopic coformer were responsible for these shifts (Fig. S5a†).

TPH form II (refcode BAPLOT06) self-assembles through N–H⋯N synthons. In a similar way, in the cocrystal **TPH-DITFB**, the self-assembly also occurred but through N–H⋯O=C interactions. This is reflected by a shift to lower frequencies of the vibrational modes corresponding to C=O and C=N stretchings, which are also involved in the halogen bond interactions (C=O(6)⋯I(2) and N(9)⋯I(1)) (as shown in Fig. 4c).

Finally, for **TBR** (refcode SEDNAQ), self-assembly occurred through N(1)–H⋯O(2)=C interactions. Despite the crystal structure not being obtained, in the FT-IR spectrum of cocrystal **TBR-DITFB** (1:1), an increase of wavenumbers corresponding to the C=O stretching was observed, suggesting that this group was also involved in the new network formed by hydrogen and halogen bonds. Finally, for the **TBR-DITFB** (2:1) cocrystal, a shift to higher wavenumbers for the C=O and imine bands was observed, due to the establishment of hydrogen and halogen bonds, as described in the previous SC-XRD section. For all these compounds, in the region 3100–2900 cm^{-1}, corresponding to N–H modes, some peak shifts were also observed and ascribed to these interactions.

Absorption and luminescence properties

In order to study the effects of cocrystallization and the molecular packing on the optical features, the absorption and emission properties of the solid compounds were studied.

Diffuse reflectance (and corresponding absorption) (DR-UV-vis) and fluorescence emission (FE) spectra of the pristine methylxanthines and their corresponding cocrystals were measured in the solid state (Fig. 6 and S6†). Both cocrystals and methylxanthines showed absorption in the UV region. In all cases, the bands of the cocrystals slightly broadened with respect to the solid pure xanthine forming a tail up to 350 nm, suggesting a variation of the intermolecular interactions in the cocrystals.

The three methylxanthines exhibited blue emission (λ_{max} = 402, 450, and 455 nm) with different absolute PL quantum yield values (Φ_{PL} = 54.7, 12.4, and 53.6%), whereas the emission considerably dropped after the formation of the corresponding cocrystals (Table 4). **CAF** showed a maximum emission band at 402 nm when excited at 350 nm, while in the cocrystal **CAF-DITFB** the emission band was slightly red-shifted to 406 nm upon excitation at
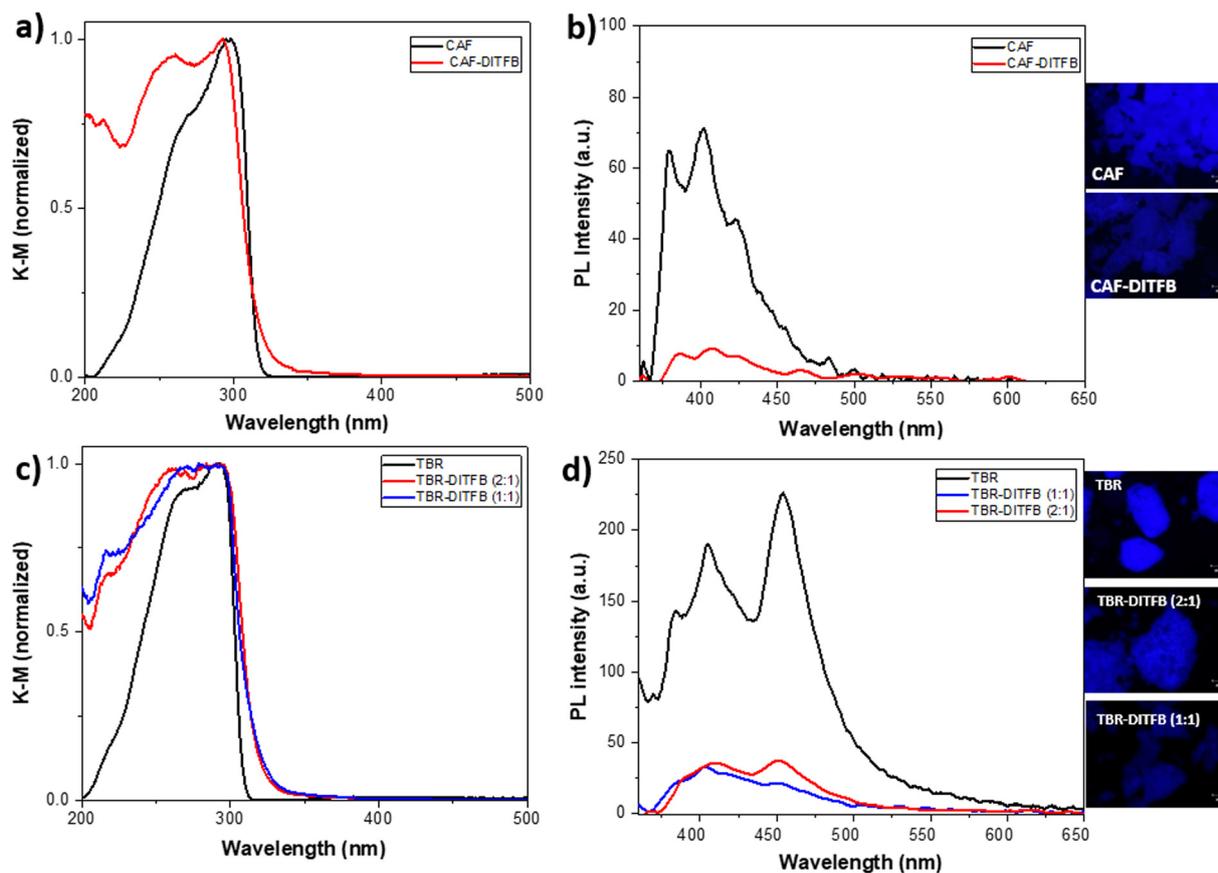
Fig. 6 Absorption and fluorescence emission spectra of **CAF** and **CAF-DITFB** cocrystals (a and b) and **TBR** and its cocrystals **TBR-DITFB** (1:1) and **TBR-DITFB** (2:1) (c and d).

345 nm (Fig. 6a). It is important to stress the significant decrease of the Φ_{PL} after the introduction of **DITFB** to form the cocrystal with respect to the pristine **CAF** (54.7% *versus* 2.4%). In the case of **TPH**, excitation at 330 nm afforded an emission band at 450 nm with a Φ_{PL} of 12.4%. The formation of the cocrystal **TPH-DITFB** produced a significant decrease of the luminescence and negligible Φ_{PL} (Table 4). Remarkably, **TBR** exhibited blue emission with a maximum at 455 nm upon excitation at 330 nm and a high Φ_{PL} value of 53.6%. Both cocrystals **TBR-DITFB** (1:1) and **TBR-DITFB** (2:1) exhibited a blue-shift of the emission bands (at around 404–406 and 449–451 nm, respectively) when compared to the pristine **TBR** and, as for the previous

cocrystals, a large decrease of the Φ_{PL} values (Table 4 and Fig. 6d). Notably, **TPH** showed much lower luminescence quantum efficiency than its analogues **CAF** and **TBR**, which in turn presented similar quantum efficiency in the solid state. The large variation of the fluorescence intensity between the pristine compounds and the corresponding crystals could be easily observed even through fluorescence microscopy images, under UV irradiation (330–385 nm range), as shown in Fig. 6 (insets).

In general, the important quenching of luminescence that occurs after the formation of the cocrystals, compared to the corresponding methylxanthines, evidences that a) the interactions between the coformer **DITFB** and the different methylxanthines are established and b) the incorporation of **DITFB** molecules in the network does not improve the luminescence properties of the methylxanthines in the solid state, probably due to the overall dilution of the intermolecular interactions among methylxanthines (*vide infra*). Furthermore, as described in the thermal analysis section, since these cocrystals display cocrystal-to-crystal transformations by heating (Fig. S4†), a new system with thermally-induced off–on luminescence modulation was achieved, which might be of interest for the optical detection of the starting natural methylxanthines in optoelectronics or biological applications.

Table 4 Photophysical properties of methylxanthines and their respective cocrystals in the solid state

	λ_{ex} (nm)	λ_{em} (nm)	Φ (%)
CAF (β polymorph)	350	402	54.7
CAF-DITFB	345	406	2.4
TPH (form II)	330	450	12.4
TPH-DITFB	350	429	<0.2
TBR	330	405, 455	53.6
TBR-DITFB (1:1)	346	404, 451	3.7
TBR-DITFB (2:1)	346	406, 449	8.2

Computational results

Periodic calculations. The optimized cell parameters are α = γ = 90° and β = 110.99° with a = 21.92 Å, b = 4.11 Å and c = 25.76 Å for **CAF-DITFB**. The computed parameter of the unit cell for **TPH-DITFB** are α = γ = 90°, β =113.37° and a = 19.82 Å, b = 4.45 Å and c = 20.36 Å. Meanwhile for **TBR-DITFB** (2 : 1) the cell parameters are α = 81.99°, β = 80.63°, γ = 88.66° and a = 4.10 Å, b = 7.42 Å and c = 20.59 Å. These results are in excellent agreement with the crystallographic data obtained for each of all three cocrystals, see Table S3.† In all three systems, the computed halogen bond interactions between methylxanthines and **DITFB** through N···I bonds are in the range from 2.80 Å to 2.96 Å, being the experimental values for the cocrystal, between 2.86 Å and 3.03 Å. Besides, the calculations reveal similar results regarding the C–I···A bond angles, which are between 174.4° and 176.6°. These values agree with the experimental crystallographic data, which are in a range from 175.4° to 177.1°, see Table S4.†

Optical properties of free methylxanthines and cocrystals

To have a benchmark for our results, the energies of the states of the isolated methylxanthines were calculated, using as references the previously reported experimental data. The UV-vis absorption spectra were calculated using the input data, the optimized structures of free methylxanthines, *i.e.*, **CAF**, **TPH** and **TBR**. From these results, we found that the main calculated absorption bands are centered at 259, 255 and 251 nm for **CAF**, **TPH** and **TBR**, respectively. The oscillator strength (f) for these transitions agrees between the simulated UV-vis absorption spectra of **CAF**, **TPH** and **TBR** and the previously reported experimental results (λ_{max} = 299, 256 and 291 nm, for **CAF**, **TPH** and **TBR**, respectively).[63,64] The observed theoretical value variations from the experimental results of around 40 nm are within the TD-DFT error range that is commonly reported.[64–66] In addition, the mentioned electronic transitions are characterized by π-type transitions, as indicated by the active molecular orbitals (see Table S5†). Thus, these three methylxanthines are characterized by π–π* transitions, which involve charge transfer (CT) between π-type molecular orbitals (MOs) with an important contribution from the nitrogen lone pairs.

Based on previous studies, we have shown how crucial it is to consider the first excited electronic states (S_1 or T_1) to accurately estimate the luminescence properties in molecular systems[66–68] and materials like MOFs.[69,70] Fig. S7† illustrates the most probable emission pathway for the free methylxanthines considering the energy of their ground and first excited electronic states. The frontier molecular orbital (FMO) analysis revealed that the MOs involved in the emissive states of the free **CAF**, **TBR** and **TPH** are located on the core of methylxanthine, *i.e.*, MOs located along the rings, both pyrimidine and imidazole, of the same monomer. Fig. S8–S10† display the FMOs of **CAF**, **TBR** and **TPH**, respectively. It should be noted that the characteristic emissive state is observed for both S_1 and T_1 electronic states.

The theoretical analysis of the optical properties of the herein studied cocrystals was performed using a finite fragment. The UV-vis absorption spectrum for **CAF-DITFB** showed two intense absorption bands, very close in energy, which appeared localized at 256 and 257 nm. The calculations showed that these bands are π-type electronic transitions. Also, it was found that the active MOs in these electronic transitions are localized on the **CAF** unit (Table S5†). However, when the FMOs of this system were analyzed, it appeared that the electron density of the lowest unoccupied molecular orbital (LUMO) is distributed on the **DITFB** unit (see Fig. S11a†). The simulated UV-vis absorption spectra of **TPH-DITFB** and **TBR-DITFB** showed their main absorption bands between 200 and 300 nm, which agree with the experimental data (see Table 5). In this sense, for both cocrystals the calculations showed that the MOs involved in this transition are localized on the xanthine moieties *i.e.*, **THP** and **TBR**, respectively, see Table S5.† The FMOs of these two cocrystals, similar to that of the **CAF-DIFTB** system, also revealed that the HOMO is located on the methylxanthine unit, *i.e.*, **TPH** and **TBR**, whereas the LUMO is a MO distributed on the **DITFB** unit (Fig. S11b and c†).

As shown for the free methylxanthines, we have also considered the most probable emission pathway for each cocrystal taking into account the electronic configuration of their S_0, S_1 and T_1, (Fig. S12†). According to the experimental emission spectra, it seemed that the incorporation of **DITFB** in the cocrystal network significantly contributed to a change in the photoluminescence of the cocrystals with respect to the free methylxanthines. Thus, for example, the quantum yield for the **CAF-DITFB** cocrystal exhibited a noticeable reduction in comparison to the free **CAF**. Therefore, we expected to see a significant contribution of **DITFB** to the **CAF-DITFB** cocrystal's luminescence properties. With this aim, the electronic configuration of the S_1 and T_1 electronic states of **CAF-DITFB** were investigated to fully understand the deactivation mechanism. The FMOs analysis of the S_1 and T_1 electronic states of the cocrystal is summarized in Fig. S12.† The single occupied molecular orbital (SOMO) is an orbital where the electron density is located on the **DITFB** unit. However, the FMO analysis showed that this excited electron relaxes to a MO distributed mostly along the **DITFB** unit and partially on the **CAF** units in both configurations (S_1 and T_1). It should be noted that the T1 electronic configuration for **CAF-DITFB** is not populated under the experimental conditions. According to Kasha's rule, the lowest excited electronic state of a given multiplicity leads to the radiative deactivation of the excited state. Therefore, in the **CAF-DITFB** system the emission drops due to a CT process, which is faster than the radiative deactivation of the excited state (implying a CT channel from the **CAF** to **DITFB** orbital). The electron relaxes after the photoexcitation process and enters the first excited electronic state, with a significant contribution from **DITFB**, which shows a weak fluorescence.[21]

Following the same procedure, the first excited states S_1 and T_1 were also investigated for the **TPH-DITFB** and **TBR-**

Table 5 Maximum absorption wavelengths (λ) and nature of singlet → singlet absorption vertical transitions simulated at the PBE0/ def2-TZVPP theoretical level

System	E_{HL}(eV)	E(eV)	λ(nm)	f	Assignment	Transition	Weight
CAF-DITFB	3.79	4.83	257	0.32	$\pi \to \pi^*$	H-1 → L + 6	(44%)
						H → L + 7	(43%)
		4.86	255	0.43	$\pi \to \pi^*$	H-3 → L + 4	(44%)
						H-2 → L + 5	(44%)
CAF	5.29	4.79	259	0.52	$\pi \to \pi^*$	H-1 → L	(90%)
TPH-DITFB	5.08	4.75	249	0.29	$\pi \to \pi^*$	H → L + 1	(84%)
TPH	5.40	4.86	255	0.23	$\pi \to \pi^*$	H → L + 1	(83%)
		4.94	251	0.18	$\pi \to \pi^*$	H-1 → L	(82%)
TBR-DITFB	5.39	4.85	255	0.67	$\pi \to \pi^*$	H-1 → L	(30%)
					$\pi \to \pi^*$	H → L + 1	(32%)
		5.18	239	0.23	$\pi \to \pi^*$	H-1 → L + 1	(70%)
TBR	4.87	4.93	251	0.14	$\pi \to \pi^*$	H-2 → L	(90%)
			247	0.28	$\pi \to \pi^*$	H → L + 2	(83%)

Excitation wavelength (λ/nm), energy (E/eV), oscillator strength (f) and the corresponding molecular orbitals (MOs) involved in the electronic transitions, as also the band assignment. The HOMO–LUMO energy differences (E_{HL}/eV) are also included.

DITFB systems. The S_1 and T_1 electronic states of these cocrystals exhibited a MO with mix distribution on **DITFB** as well as the **TPH** and **TBR** molecules, as observed before for **CAF-DITFB**, see Fig. S14 and S15.†

Based on these results, as well as the Franck–Condon principle, Kasha's rule, and selection rules, we propose that the MO composition of the first excited electronic state involves MOs distributed mostly on the **DITFB** unit and with a minor component on the methylxanthines in the emissive state. This phenomenon contributes to a luminescence quenching effect, highlighting the significant impact of **DITFB** on the modulation of the emission in the studied cocrystals. These findings shed light on the interaction of molecular components and provide valuable insights for further understanding of the factors influencing luminescence in this system. These results lead us to the conclusion that incorporation of **DITFB** does not favor the emission process in these cocrystals, producing luminescence quenching.

Conclusions

Over the past few years, we have paid attention to the preparation of cocrystals and salts of active pharmaceutical ingredients or structural synthons mostly based on hydrogen-bonds, with interest in the pharmaceutical industry. Herein, we have reported the synthesis and characterization of new halogen bonded cocrystals based on three natural methylxanthines, caffeine, theophylline and theobromine, and the well-known 1,4-diiodotetrafluorobenzene. The several stoichiometric ratios obtained for these cocrystals (1:1 for **TPH-DITFB**, 1:1 and 2:1 for **TBR-DITFB** and 4:1 for **CAF-DITFB**) remark the importance of continuing exploration of these types of multicomponent solid forms and their physicochemical properties. Although the fluorescence of the prepared new cocrystals is greatly diminished probably as a consequence of the molecular packing and interactions with the coformer, the isolated methylxanthines have interestingly

revealed excellent luminescence properties with high PL quantum yields in the solid state. This suggests that methylxanthines can be considered suitable candidates for future luminescent materials as they are industrially produced and readily available. Moreover, our cocrystals displayed cocrystal-to-crystal transformations by heating and represent a new thermally-induced off–on luminescent system, allowing for solid thermofluorescent switches and the identification of these precursors. Furthermore, by means of TD-DFT calculations, the decrease of the photoemission observed with respect to the free methylxanthines and the herein proposed cocrystals seems to indicate that this effect was due to the generation of a molecular orbital in the excited electronic state configuration with a mixed composition of **DITFB**, as the major component, and the corresponding methylxanthine. Therefore, the introduction of **DITFB** does not enhance the emission process within these cocrystals, due to the possible CT process between the methylxanthine and the coformer.

Author contributions

The manuscript was written through contributions of all authors. All authors have given approval to the final version of the manuscript.

Conflicts of interest

There are no conflicts to declare.

Acknowledgements

References

1 X. Fernando Gomollón-Bel, Ten Chemical Innovations That Will Change Our World, *Chemistry International*, 2019, **41**(2), 12–17, DOI: **10.1515/ci-2019-0203**.

2 J. L. Howard, Q. Cao and D. L. Brown, Mechanochemistry as an emerging tool for molecular synthesis: what can it offer?, *Chem. Sci.*, 2018, **9**(12), 3080–3094, DOI: **10.1039/C7SC05371A**.

3 S. Hwang, S. Grätz and L. Borchardt, A guide to direct mechanocatalysis, *Chem. Commun.*, 2022, **58**, 1661–1671, DOI: **10.1039/D1CC05697B**.

4 D. Braga, L. Maini and F. Grepioni, Mechanochemical preparation of co-crystals, *Chem. Soc. Rev.*, 2013, **42**, 7638–7648, DOI: **10.1039/C3CS60014A**.

5 G. Bolla and A. Nangia, Pharmaceutical cocrystals: walking the talk, *Chem. Commun.*, 2016, **52**, 8342–8360, DOI: **10.1039/C6CC02943D**.

6 G. R. Desiraju, P. S. Ho, L. Kloo, A. C. Legon, R. Marquardt, P. Metrangolo, P. Politzer, G. Resnati and K. Rissanen, Definition of the halogen bond (IUPAC Recommendations 2013), *Pure Appl. Chem.*, 2013, **85**, 1711–1713, DOI: **10.1351/PAC-REC-12-05-10**.

7 P. Auffinger, F. A. Hays, E. Westhof and P. S. Ho, Halogen bonds in biological molecules, *Proc. Natl. Acad. Sci. U. S. A.*, 2004, **101**, 16789–16794, DOI: **10.1073/pnas.0407607101**.

8 V. Govindaraj, H. Ungati, S. Jakka, S. Bose and G. Mugesh, Directing traffic: halogen-bond-mediated membrane transport, *Chem. – Eur. J.*, 2019, **25**, 11180–11192, DOI: **10.1002/chem.201902243**.

9 Y. Roselló, N. Bagués, N. Martínez, A. Moradell, M. Benito, I. Mata, J. Galcerà, M. Barceló-Oliver, A. Frontera and E. Molins, 9-Ethyladenine: Mechanochemical Synthesis, Characterization, and DFT Calculations of Novel Cocrystals and Salts, *Cryst. Growth Des.*, 2020, **20**, 2985–2997, DOI: **10.1021/acs.cgd.9b01628**.

10 Y. Roselló, M. Benito, E. Molins, M. Barceló-Oliver and A. Frontera, Adenine as a Halogen Bond Acceptor: A Combined Experimental and DFT Study, *Crystals*, 2019, **9**, 224, DOI: **10.3390/cryst9040224**.

11 Y. Roselló, M. Benito, M. Barceló-Oliver, A. Frontera and E. Molins, 1-Ethyluracil, a New Scaffold for Preparing Multicomponent Forms. Synthesis, Characterization and Computational Studies, *Cryst. Growth Des.*, 2021, **21**, 4857–4870, DOI: **10.1021/acs.cgd.1c00175**.

12 M. Benito, Y. Roselló, M. Barceló-Oliver, A. Frontera and E. Molins, Uracil Derivatives for Halogen-bonded Cocrystals, *Int. J. Mol. Sci.*, 2021, **22**, 10663, DOI: **10.3390/ijms221910663**.

13 N. Singh, A. K. Shreshtha, M. S. Thakur and S. Patra, Xanthine scaffold: scope and potential in drug development, *Heliyon*, 2018, **4**, e00829, DOI: **10.1016/j.heliyon.2018.e00829**.

14 A. M. Comer, C. M. Perry and D. P. Figgitt, Caffeine citrate. A review of its use in apnoea of prematurity, *Paediatr. Drugs*, 2001, **3**(1), 61–79, DOI: **10.2165/00128072-200103010-00005**.

15 W. Martindale, *The Extra Pharmacopoeia*, 30th edn, 1993, pp. 1318–1319.

16 S. Sinha, Z. Kelemen, E. Hümpfner, I. Ratera, J.-P. Malval, J. P. Jurado, C. Viñas, F. Teixidor and R. Núñez, O-Carboran-based fluorophores as efficient luminescent systems both as solids and as water-dispersible nanoparticles, *Chem. Commun.*, 2022, **58**, 4016–4019, DOI: **10.1039/D1CC07211K**.

17 J. R. Otaegui, A. Carracull-Marín, D. Ruiz-Molina, J. Hernando and C. Roscini, Multimodal fluorescence switching materials: one dye to have them all, *Adv. Opt. Mater.*, 2022, **10**, 2200083, DOI: **10.1002/adom.202200083**.

18 D. Yan, A. Delori, G. O. Lloyd, T. Friščić, G. M. Day, W. Jones, J. Lu, M. Wei, D. G. Evans and X. Duan, A cocrystal strategy to tune the luminescent properties of stilbene-type organic solid-state materials, *Angew. Chem., Int. Ed.*, 2011, **50**, 12483–12486, DOI: **10.1002/anie.201106391**.

19 J. D. Wuest, Co-crystals give light a tune-up, *Nat. Chem.*, 2012, **4**, 74–75, DOI: **10.1038/nchem.1256**.

20 D. Yan and D. G. Evans, Molecular crystalline materials with tunable luminescent properties: from polymorphs to multi-component solids, *Mater. Horiz.*, 2014, **1**, 46–57, DOI: **10.1039/C3MH00023K**.

21 W. Zhu, R. Zheng, Y. Zhen, Z. Yu, H. Dong, H. Fu, Q. Shi and W. Hu, Rational design of charge-transfer interactions in halogen-bonded co-crystals toward versatile solid-state optoelectronics, *J. Am. Chem. Soc.*, 2015, **137**(34), 11038–11046, DOI: **10.1021/jacs.5b05586**.

22 Y. Huang, Q. Gong, J. Ge, P. Tang, F. Yu, L. Xiao, Z. Wang, H. Sun, J. Yu, D.-S. Li, Q. Xiong and Q. Zhang, Green grinding-coassembly engineering toward intrinsically luminescent tetracene in cocrystals, *ACS Nano*, 2020, **14**, 15962–15972, DOI: **10.1021/acsnano.0c07416**.

23 M. Singh, K. Liu, S. Qu, H. Ma, H. Shi, Z. An and W. Huang, Recent advances of cocrystals with room temperature phosphorescence, *Adv. Opt. Mater.*, 2021, **9**, 2002197, DOI: **10.1002/adom.202002197**.

24 L. Sun, W. Zhu, X. Zhang, L. Li, H. Dong and W. Hu, Creating organic functional materials beyond chemical bond synthesis by organic cocrystal engineering, *J. Am. Chem. Soc.*, 2021, **143**, 19243–19256, DOI: **10.1021/jacs.1c07678**.

25 S. D'Agostino, F. Spineeli, P. Taddei, B. Ventura and F. Grepioni, Ultralong organic phosphorescence in the solid state: the case study of triphenylene cocrystals with halo- and dihalo-penta/tetrafluorobenzene, *Cryst. Growth Des.*, 2019, **19**, 336–346, DOI: **10.1021/acs.cgd.8b01443**.

26 A. Azzali, S. d'Agostino, M. Capacci, F. Spinelli, B. Ventura and F. Grepioni, Assembling photoactive materials from polycyclic aromatic hydrocarbons (PAHs): room temperature phosphorescence and excimer-emission in co-crystals with 1,4-diiodotetrafluorobenzene, *CrystEngComm*, 2022, **24**, 5748–5756, DOI: **10.1039/D2CE00720G**.

27 M. M. Andino, C. G. de Lima and J. D. Winefordner, Luminescence characteristics of caffeine and theophylline, *Spectrochim. Acta, Part A*, 1987, **43**, 427–437, DOI: **10.1016/0584-8539(87)80129-0**.

28 M. D. Gaye and J. J. Aaron, The effect of pH on the room-temperature phosphorescence properties of several purine and pyrimidine derivatives, *Talanta*, 1989, **36**, 445–449, DOI: **10.1016/0039-9140(89)80226-7**.

29 D. H. Murgida and R. Erra-Balsells, Low-temperature luminescence of purine derivatives: salt effects, *J. Lumin.*, 1999, **85**, 129–136, DOI: **10.1016/S0022-2313(99)00059-9**.

30 D. Chuan, W. Yan-Li and S. Shao-Min, Study on the paper substrate room temperature phosphorescence of theobromine, caffeine and theophylline and analytical application, *Spectrochim. Acta, Part A*, 2003, **59**, 1469–1476, DOI: **10.1016/s1386-1425(02)00359-1**.

31 Y.-L. Wei, C. Dong, S.-M. Shuan and D.-S. Liu, Study for luminescence performance of three methyl xanthine derivatives, *Spectrochim. Acta, Part A*, 2005, **61**, 2584–2589, DOI: **10.1016/j.saa.2004.09.024**.

32 P. Changenet-Barret, L. Kovács, D. Markovitsi and T. Gustavsson, Xanthines studied via femtosecond fluorescence spectroscopy, *Molecules*, 2016, **21**, 1668, DOI: **10.3390/molecules21121668**.

33 A. Camiruaga, I. Usabiaga, V. C. D'mello, G. A. García, S. Watergaonkar and J. A. Fernández, Revisiting the spectroscopy of xanthine derivatives: theobromine and theophylline, *Phys. Chem. Chem. Phys.*, 2019, **21**, 26430, DOI: **10.1039/C9CP05068J**.

34 J. Tan, R. Li, Z.-T. Jiang, S.-H. Tang and Y. Wang, Rapid and non-destructive prediction of methylxanthine and cocoa solid contents in dark chocolate by synchronous front-face fluorescence spectroscopy and PLSR, *J. Food Compos. Anal.*, 2019, **77**, 20–27, DOI: **10.1016/j.jfca.2019.01.001**.

35 Y. Huang, Y. Liu, P. J. W. Sommerville, W. Kaminsky, D. S. Ginger and C. K. Luscombe, Theobromine and direct arylation: a sustainable and scalable solution to minimize aggregation caused quenching, *Green Chem.*, 2019, **21**, 6600, DOI: **10.1039/C9GC03391B**.

36 Y. Huang, T. A. Cohen and C. K. Luscombe, Green syntheses of stable and efficient organic dyes for organic hybrid light-emitting diodes, *J. Mater. Chem. C*, 2021, **135**, 1085, DOI: **10.1039/D1TC01567B**.

37 C. W. Lehmann and F. Stowasser, The crystal structure of anhydrous β-caffeine as determined from X-ray powder diffraction data, *Chem. – Eur. J.*, 2007, **13**, 2908–2911, DOI: **10.1002/chem.200600973**.

38 Y. Ebisuzaki, P. D. Boyle and J. A. Smith, Methylxanthines. I. Anhydrous Theophylline, *Acta Crystallogr., Sect. C: Cryst. Struct. Commun.*, 1997, **53**, 775–777, DOI: **10.1107/S0108270197000516**.

39 K. A. Ford, Y. Ebisuzaki and P. D. Boyle, Methylxanthines. II. Anhydrous Theobromine, *Acta Crystallogr., Sect. C: Cryst. Struct. Commun.*, 1998, **54**, 1980–1983.

40 R. H. Blessing, An empirical correction for absorption anisotropy, *Acta Crystallogr., Sect. A: Found. Crystallogr.*, 1995, **51**, 33–38, DOI: **10.1107/S0108767394005726**.

41 *SAINT*, Bruker A.X.S. Inc., Madison, Wisconsin, USA.

42 G. M. Sheldrick, SHELXT-Integrated space-group and crystal-structure determination, *Acta Crystallogr., Sect. A: Found. Adv.*, 2015, **71**, 3–8, DOI: **10.1107/S2053273314026370**.

43 G. M. Sheldrick, Crystal structure refinement with Shelxl, *Acta Crystallogr., Sect. C: Struct. Chem.*, 2015, **71**, 3–8, DOI: **10.1107/s2053229914024218**.

44 L. J. Farrugia, WinGX and ORTEP for Windows: an update, *J. Appl. Crystallogr.*, 2012, **45**, 849–854, DOI: **10.1107/S0021889812029111**.

45 C. F. Macrae, I. J. Bruno, J. A. Chisholm, P. R. Edgington, P. McCabe, E. Pidcock, L. Rodriguez-Monge, R. Taylor, J. van de Streek and P. A. Wood, Mercury CSD 2.0-new features for the visualization and investigation of crystal structures, *J. Appl. Crystallogr.*, 2008, **41**, 466–470, DOI: **10.1107/S0021889807067908**.

46 M. Ernzerhof and G. E. Scuseria, Assessment of the Perdew-Burke-Ernzerhof exchange-correlation functional, *J. Chem. Phys.*, 1999, **110**, 5029–5036, DOI: **10.1063/1.478401**.

47 A. Dal Corso, Pseudopotentials periodic table: From H to Pu, *Comput. Mater. Sci.*, 2014, **95**, 337–350, DOI: **10.1016/j.commatsci.2014.07.043**.

48 S. Grimme, S. Ehrlich and L. Goerigk, Effect of the damping function in dispersion corrected density functional theory, *J. Comput. Chem.*, 2011, **32**, 1456–1465, DOI: **10.1002/jcc.21759**.

49 P. Giannozzi, S. Baroni, N. Bonini, M. Calandra, R. Car and C. Cavazzoni, *et al.* QUANTUM ESPRESSO: a modular and open-source software project for quantum simulations of materials, *QUANTUM ESPRESSO 2*, 2009.

50 P. Giannozzi, O. Andreussi, T. Brumme, O. Bunau, M. Buongiorno Nardelli and M. Calandra, *et al.* Advanced capabilities for materials modelling with Quantum ESPRESSO, *J. Phys.: Condens. Matter*, 2017, **29**, 465901, DOI: **10.1088/1361-648X/aa8f79**.

51 F. Neese, The ORCA program system, *Wiley Interdiscip. Rev. Comput. Mol. Sci.*, 2012, **2**, 73–78, DOI: **10.1002/wcms.81**.

52 J. P. Perdew, K. Burke and M. Ernzerhof, Generalized gradient approximation made simple, *Phys. Rev. Lett.*, 1996, **77**, 3865–3868, DOI: **10.1103/PhysRevLett.77.3865**.

53 F. Weigend and R. Ahlrichs, Balanced basis sets of split valence, triple zeta valence and quadruple zeta valence quality for H to Rn: Design and assessment of accuracy, *Phys. Chem. Chem. Phys.*, 2005, **7**, 3297–3305, DOI: **10.1039/b508541a**.

54   F. Weigend, Accurate Coulomb-fitting basis sets for H to Rn, *Phys. Chem. Chem. Phys.*, 2006, **8**, 1057–1065, DOI: **10.1039/b515623h.**

55   F. Neese, F. Wennmohs, A. Hansen and U. Becker, Efficient, approximate and parallel Hartree-Fock and hybrid DFT calculations. A "chain-of-spheres" algorithm for the Hartree-Fock exchange, *Chem. Phys.*, 2009, **356**, 98–109, DOI: **10.1016/j.chemphys.2008.10.036.**

56   G. L. Stoychev, A. A. Auer and F. Neese, Automatic Generation of Auxiliary Basis Sets, *J. Chem. Theory Comput.*, 2017, **13**, 554–562, DOI: **10.1021/acs.jctc.6b01041.**

57   C. Adamo and V. Barone, Toward reliable density functional methods without adjustable parameters: The PBE0 model, *J. Chem. Phys.*, 1999, **110**, 6158–6170, DOI: **10.1063/1.478522.**

58   D. R. Lide, *CRC Handbook of Chemistry and Physics*, CRC Press, Boca Raton, FL, 2016.

59   M. Gołdyn, D. Larowska, W. Nowak and E. Bartoszak-Admska, Synthon hierarchy in theobromine cocrystals with hydroxybenzoic acids as coformers, *CrystEngComm*, 2019, **21**, 7373–7388, DOI: **10.1039/C9CE01195A.**

60   B. Saikia, D. Pathak and B. Sarma, Variable stoichiometry cocrystals: occurrence and significance, *CrystEngComm*, 2021, **23**, 4583–4606, DOI: **10.1039/D1CE00451D.**

61   C. Zhao, W. Li, Z. Li, W. Hu, S. Zhang and S. Wu, Preparation and solid-state characterization of dapsone pharmaceutical cocrystals through supramolecular synthon strategy, *CrystEngComm*, 2021, **23**, 6690–6702, DOI: **10.1039/D1CE00945A.**

62   H. Abourahma, D. D. Shah, J. Melendez, E. J. Johnson and K. T. Holman, A Tale of Two Stoichiometrically Diverse Cocrystals, *Cryst. Growth Des.*, 2015, **15**, 3101–3104, DOI: **10.1021/acs.cgd.5b00357.**

63   G. V. S. Mota and A. M. J. C. Neto, Theoretical UV spectroscopy proprieties of methylxanthines, *J. Comput. Theor. Nanosci.*, 2010, **7**, 205–208, DOI: **10.1166/jctn.2010.1346.**

64   S. Gómez, T. Giovannini and C. Cappelli, Absorption spectra of xanthines in aqueous solution: A computational study, *Phys. Chem. Chem. Phys.*, 2020, **22**, 5929–5941, DOI: **10.1039/c9cp05420k.**

65   R. Ramakrishnan, M. Hartmann, E. Tapavicza and O. A. Von Lilienfeld, Electronic Spectra from TDDFT and Machine Learning in Chemical Space, *J. Chem. Phys.*, 2015, **143**, 084111, DOI: **10.1063/1.4928757.**

66   M. A. Treto-Suárez, Y. Hidalgo-Rosa, E. Schott, X. Zarate and D. Páez-Hernández, Understanding the Selective-Sensing Mechanism of Al 3+ Cation by a Chemical Sensor Based on Schiff Base: A Theoretical Approach, *J. Phys. Chem. A*, 2019, **123**, 6970–6977, DOI: **10.1021/acs.jpca.9b03366.**

67   M. A. Treto-Suárez, Y. Hidalgo-Rosa, E. Schott, X. Zarate and D. Páez-Hernández, Radiative decay channel assessment to understand the sensing mechanism of a fluorescent turn-on Al3+ chemosensor, *Int. J. Quantum Chem.*, 2020, **120**, 26083, DOI: **10.1002/qua.26083.**

68   M. A. Treto-Suárez, Y. Hidalgo-Rosa, E. Schott, D. Páez-Hernández and X. Zarate, Fluorescence turn-on and turn-off mechanisms of a dual-selective chemosensor of Bi3+ and pH changes: Insights from a theoretical perspective, *Dyes Pigm.*, 2021, **185**, 108934, DOI: **10.1016/j.dyepig.2020.108934.**

69   Y. Hidalgo-Rosa, M. A. Treto-Suárez, E. Schott, X. Zarate and D. Páez-Hernández, Sensing mechanism elucidation of a chemosensor based on a metal-organic framework selective to explosive aromatic compounds, *Int. J. Quantum Chem.*, 2020, 120, DOI: **10.1002/qua.26404.**

70   Y. Hidalgo-Rosa, K. Mena-Ulecia, M. A. Treto-Suárez, E. Schott, D. Páez-Hernández and X. Zarate, Insights into the selective sensing mechanism of a luminescent Cd(II)-based MOF chemosensor toward NACs: roles of the host–guest interactions and PET processes, *J. Mater. Sci.*, 2021, **56**, 13684–13704, DOI: **10.1007/s10853-021-06196-3.**